Supplementary Information

Highly Efficient Light-Driven Methane Coupling at Ambient Condition Based on Integrated Design of Photocatalytic System

Junyu Lang[a], Yuli Ma[a], Xuechen Wu[a], Yueyue Jiang[a], and Yun Hang Hu[a,b]*

a School of Environmental Science and Engineering, Shanghai Jiao Tong University, Shanghai 200240, P. R. China

b Department of Materials Science and Engineering, Michigan Technological University, Houghton, Michigan 49931, United States

* Corresponding Author: E-mail: yunhangh@mtu.edu

Table of Contents

1. Comparison of different catalysts for photocatalytic NOCM

Table S1. Results of photocatalytic NOCM over different catalysts.

Catalysts	Light source	Type of reactor	C_2H_6 yield (umol g^{-1} h^{-1})	Selectivity (%)	reference
TiO_2 (P25)	Simulated sunlight, 100 mW/cm^2	continuous flow	1.55	95.12	This work
Au/TiO_2	Simulated sunlight, 100 mW/cm^2	continuous flow	81.74	95.90	This work
Ag/TiO_2	Simulated sunlight, 100 mW/cm^2	continuous flow	37.92	96.24	This work
Pd/TiO_2	Simulated sunlight, 100 mW/cm^2	continuous flow	14.42	95.77	This work
Pt/TiO_2	Simulated sunlight, 100 mW/cm^2	continuous flow	4.05	96.09	This work
Rh/TiO_2	Simulated sunlight, 100 mW/cm^2	continuous flow	0.77	95.85	This work
Ru/TiO_2	Simulated sunlight, 100 mW/cm^2	continuous flow	18.34	95.75	This work
Ir/TiO_2	Simulated sunlight, 100 mW/cm^2	continuous flow	7.51	96.04	This work
Cu polymeric carbon nitride	Xe 500W	slurry	13.9	32.3	1
Pt/TiO_2 (Pt 0.5 %)	UV 254 nm	slurry	51 (with aid of H_2O) 400	60	2
SiO_2/Al_2O_3	250W Xe	batch	0.1	78	3
SiO_2/Al_2O_3	Simulated sunlight, 100 mW/cm^2	continuous flow	trace	-	This work
HMOR	250W Xe	batch	0.07	91	4
SiO_2/Al_2O_3/ TiO_2	250W Xe	batch	1.33	82	5
MgO/SiO_2	300W Xe	batch	4.4	97	6
FSM-16	300W Xe	batch	0.3	98.2	7
MCM-41		batch	0.14	90	
β-Ga_2O_3 [a]	300W Xe	batch	1.73	78.2	8
Ce/SiO_2	300W Xe	batch	0.77	97	9
Ce/Al_2O_3		batch	0.98	98	
Ce/SiO_2	Simulated sunlight, 100 mW/cm^2	continuous flow	0.31	91	This work
Ce/Al_2O_3	Simulated sunlight, 100 mW/cm^2	continuous flow	n.d.	-	This work
Ga_2O_3-K	300W Xe	batch	13.3	96	10
(Zn^+,Zn^{2+})-ZSM-5	Hg lamp	batch	9.8	99.6	11
Ga-ETS	150 W, Hg lamp	batch	29.8	(C_2 to C_4) with a selectivity larger than 70%	12
Au/ZnO	300 W Xe	batch	11.1	Not mentioned	13
Au/ZnO	Simulated sunlight, 100 mW/cm^2	continuous flow	6.48	95.45	This work

[a] photocatalytic reaction at 200 °C

2. Digital photograph of the test unit for photocatalytic NOCM

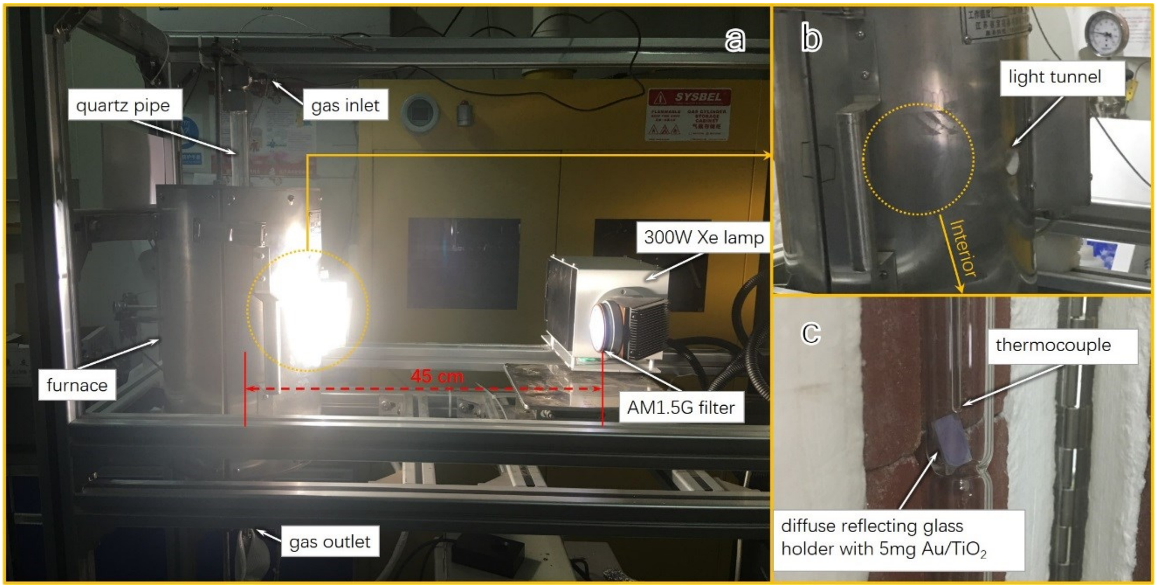

Fig. S1. The photograph of the test unit: (a) whole-unit photograph (the distance between light source and catalyst was set to 45 cm); (b) The feature of the light tunnel; (c) The reactor equipped diffuse reflecting glass holder with 5mg Au/TiO_2. A thermocouple was used to monitor the temperature of the catalyst during photocatalytic NOCM.

3. The actual loading of the M in the M-TiO_2 catalysts

Table S2. ICP-OES analysis results of all M-TiO_2 samples.*

M/TiO_2	theoretically calculated M content (%)	Actual M content (%) (determined by ICP-OES)
Au/TiO_2	0.1	0.022
Au/TiO_2	0.2	0.049
Au/TiO_2	0.5	0.19
Au/TiO_2	1.0	0.50
Au/TiO_2	1.5	0.78
Ag/TiO_2	1.0	0.73
Ir/TiO_2	1.0	0.39
Pt/TiO_2	1.0	0.52
Rh/TiO_2	1.0	0.15
Pd/TiO_2	1.0	0.34
Ru/TiO_2	1.0	0.43

* M-TiO_2 M=Au, Ag, Ir, Pt, Rh, Pd and Ru.

4. Potential drops in M-TiO_2 interface

Table S3. Potential drop (ΔV_H) in M-TiO_2 interface region*

Catalysts	Potential drop (eV) in M-TiO_2 interface region
Au/TiO_2	13.42
Ag/TiO_2	14.45
Ir/TiO_2	14.73
Pt/TiO_2	16.74
Rh/TiO_2	22.54
Pd/TiO_2	32.97

* Calculate from Fig.3 ~ Fig.10 in ref. [14]

5. Photoluminescence emission spectra

PL emission spectra were obtained for TiO_2 and Au/TiO_2 with 365 nm excitation. As shown in Fig. S1, the Au/TiO_2 displayed a much weaker peak around 560 nm than the pure TiO_2, indicating an electron–hole recombination rate in Au/TiO_2.

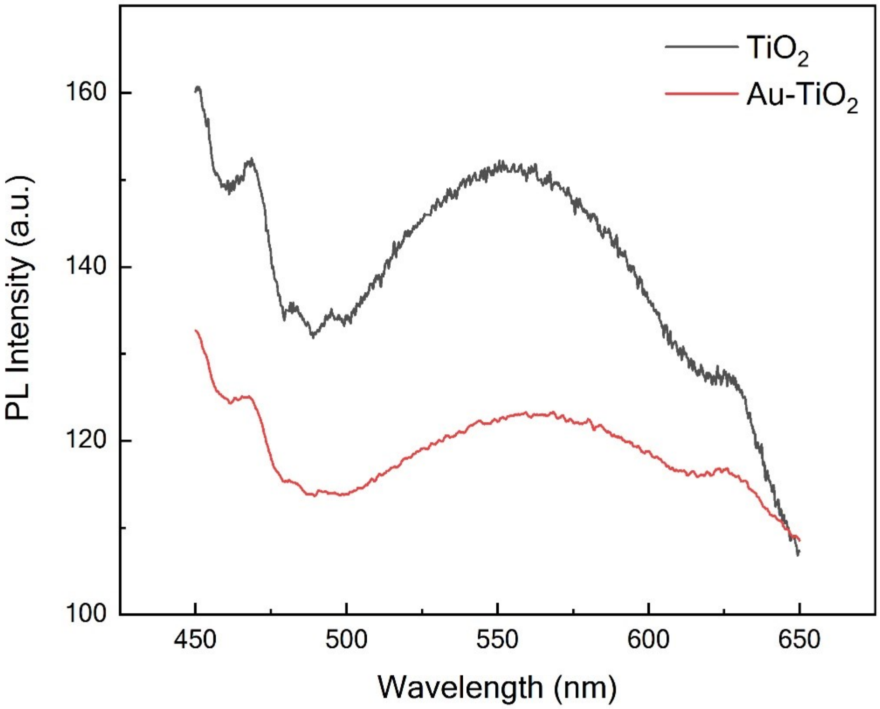

Fig. S2. Photoluminescence emission spectra of Au/TiO_2 and TiO_2 (P25).

6. The ratio between H_2 and C_2H_6 produced from the photocatalytic NOCM reaction over Au-TiO_2

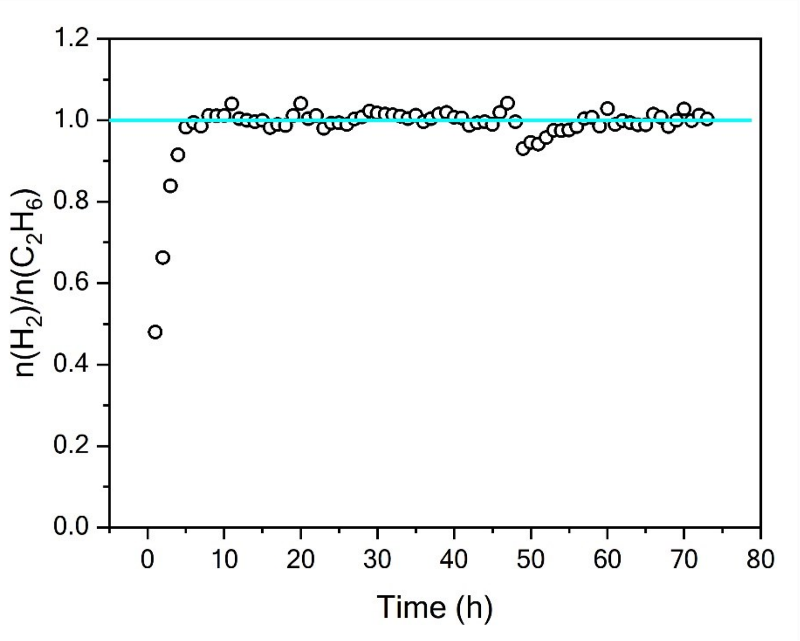

Fig. S3. The ratio of n(H2)/n(C2H6) calculated from Fig. 2c.

7. The gas chromatographs for the products

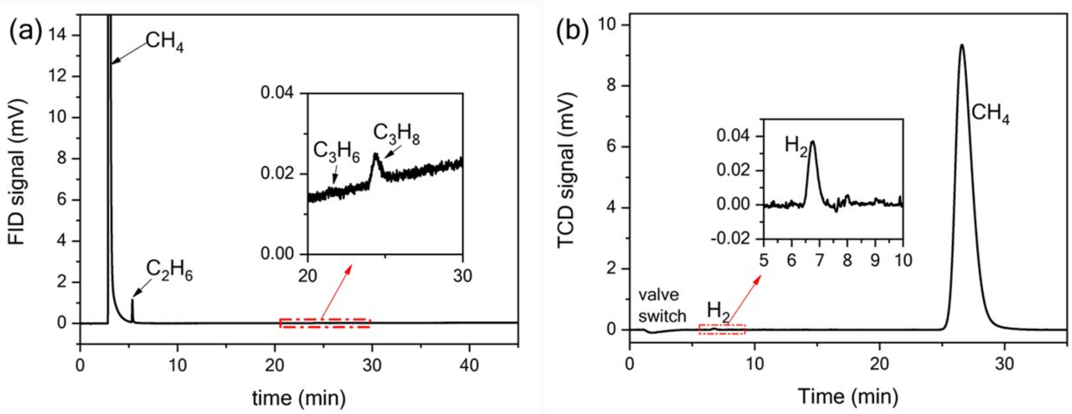

Fig. S4. The gas chromatographs for the products of photocatalytic NOCM reaction over Au-TiO_2. FID detector (a) and TCD detector (b) were used to analyzed the hydrocarbons and hydrogen, respectively.

8. Comparison of surfaces of catalyst substrates for photocatalytic NOCM

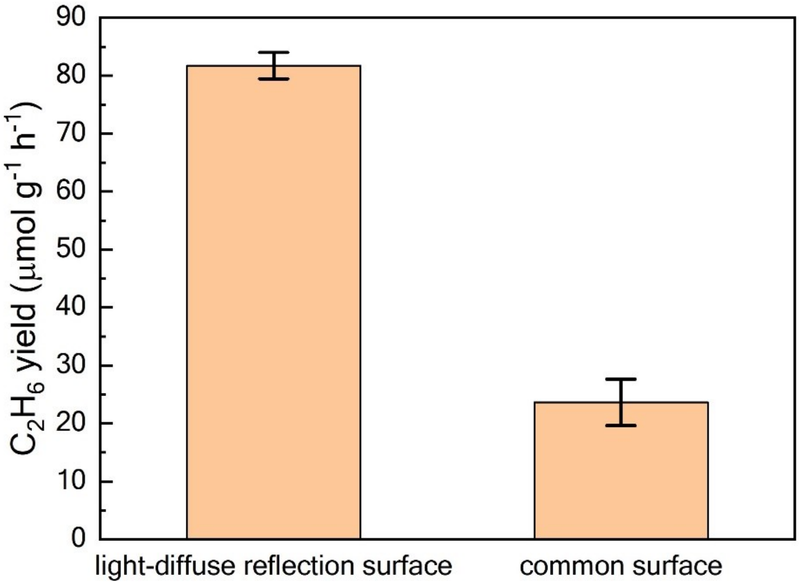

Fig. S5. C_2H_6 yield from photocatalytic NOCM over Au/TiO_2 dispersed on the light-diffuse-reflection-surface and the common-surface under simulated AM 1.5G solar light irradiation at room temperature.

9. Effect of reactor types for photocatalytic NOCM over Au/TiO_2

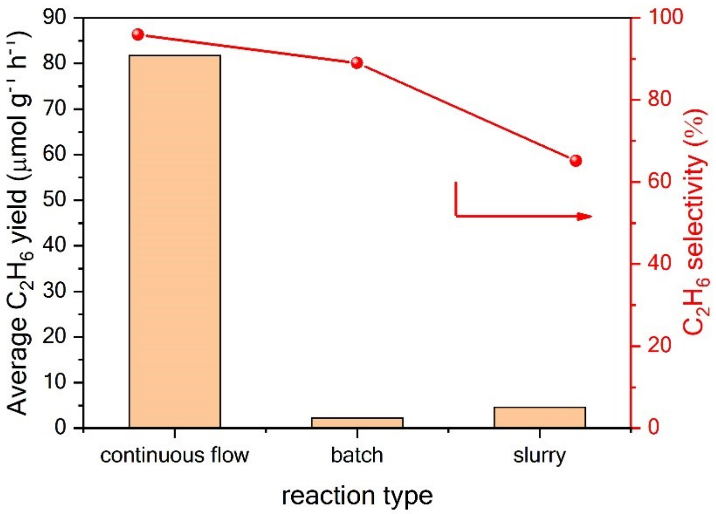

Fig. S6. Average C_2H_6 yield from methane coupling in first 8hours over Au-TiO_2 dispersed on light-diffuse-reflection surface in different reactors under simulated AM 1.5G solar light irradiation at room temperature.

10. Photocatalytic NOCM comparison between Au/TiO_2 dispersed on the light-reflection-diffuse-surface and on the common surface

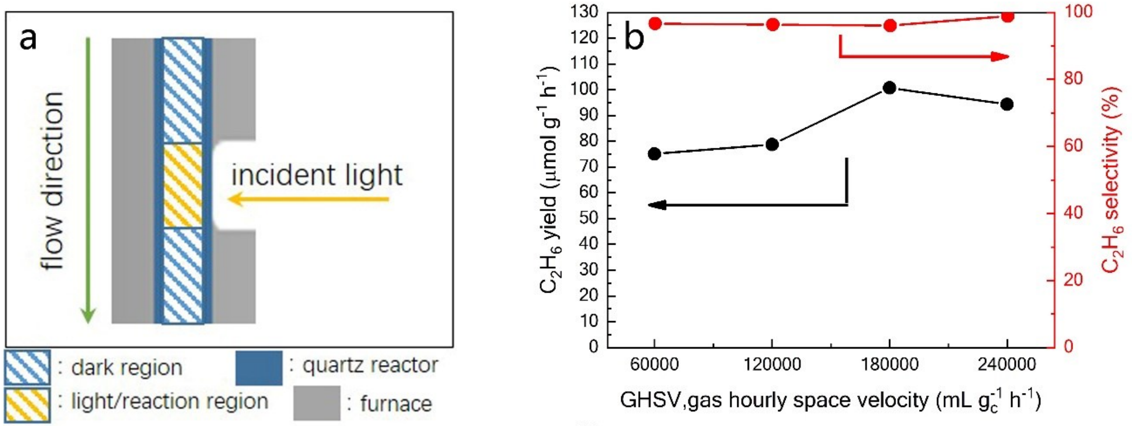

Fig. S7. (a) Schematic diagram of the reaction region in a continuous flow reactor, and (b) The effect of reactant flow rate on photocatalytic NOCM over Au/TiO_2 under simulated AM 1.5G solar light irradiation at room temperature.

11. Characterization results of catalysts

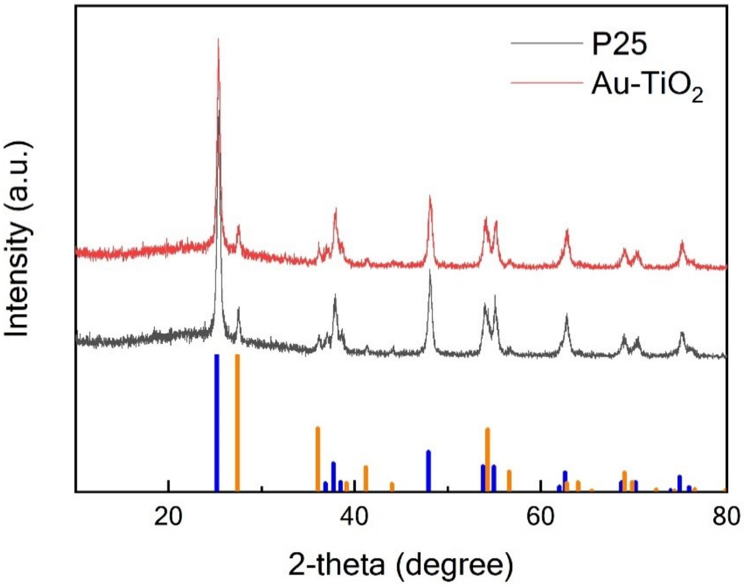

Fig. S8. XRD patterns of Au/TiO$_2$ and TiO$_2$ (P25). The blue vertical bar represents the PDF#84-1285 of anatase; the orange vertical bar represents the PDF#73-1765 of rutile. The crystallite sizes of the sample are about 23 nm calculated from the FWHM of 25.4^o by Scherrer formula.

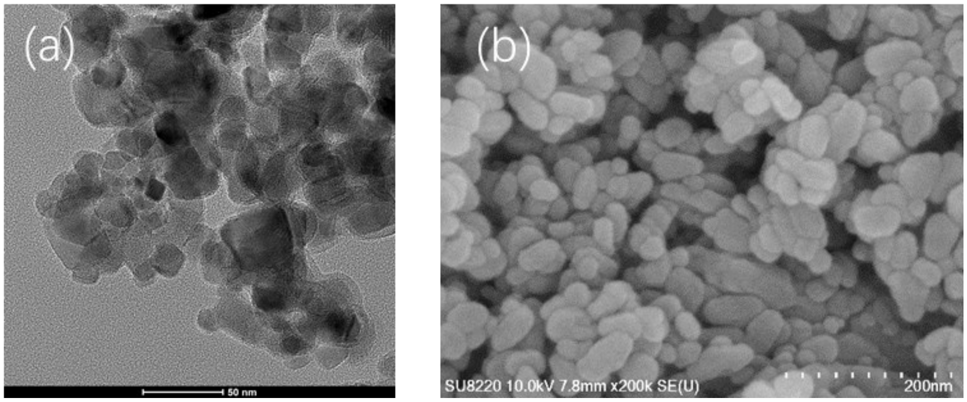

Fig. S9. TEM (a) and SEM (b) images of the Au/TiO$_2$ powders. The particles size of TiO$_2$ are about 25 nm that is consistent with the XRD results.

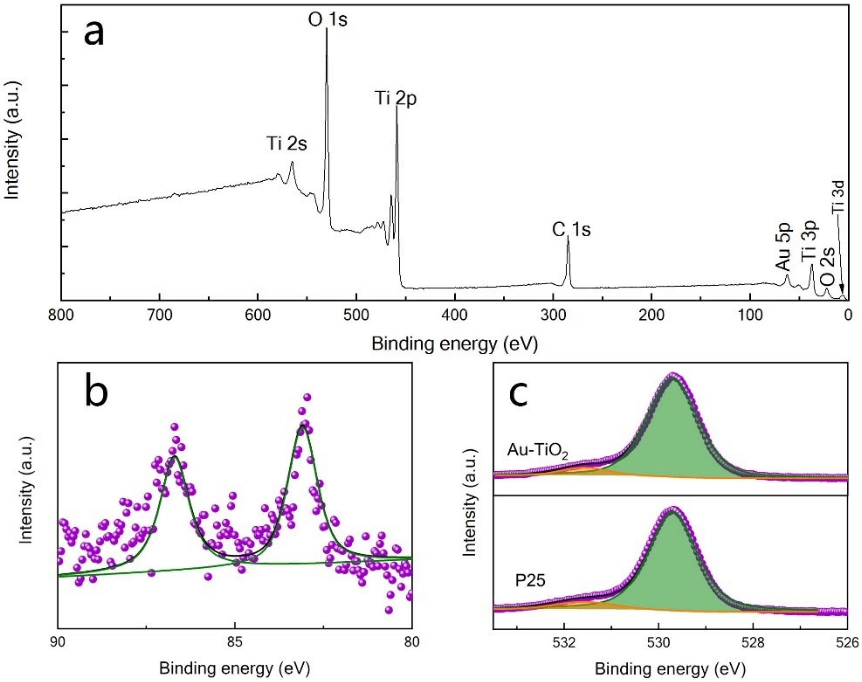

Fig. S10. XPS spectra of Au/TiO$_2$: (**a**) Survey, (**b**) Au 4f spectrum, and (**c**) O1s spectrum. The data was fitted into one set of peaks at 83.09 eV and 86.70 eV attributed to the 4f$_{7/2}$ and 4f$_{5/2}$ of Au^0 species, respectively. The gold ions were reduced to zero valence during the photo deposition process.

12. Role of photogenerated holes

To clarify whether the photo-generated hole participated in the NOCM reaction, methanol was introduced as a hole scavenger. The reaction was suppressed when the hole was trapped by methanol, indicating that the holes played a vital role in this photocatalytic process (Fig. S11).

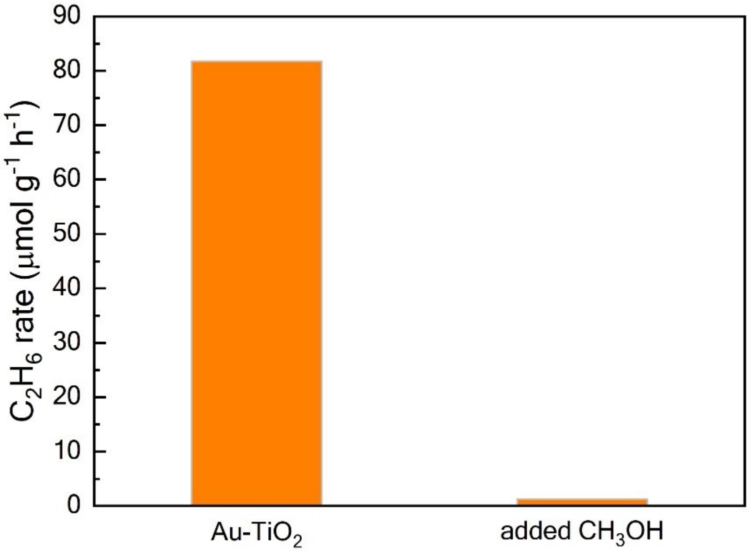

Fig. S11. The photocatalytic NOCM performance over Au/TiO_2 in the presence of CH_3OH.

13. Modeling results

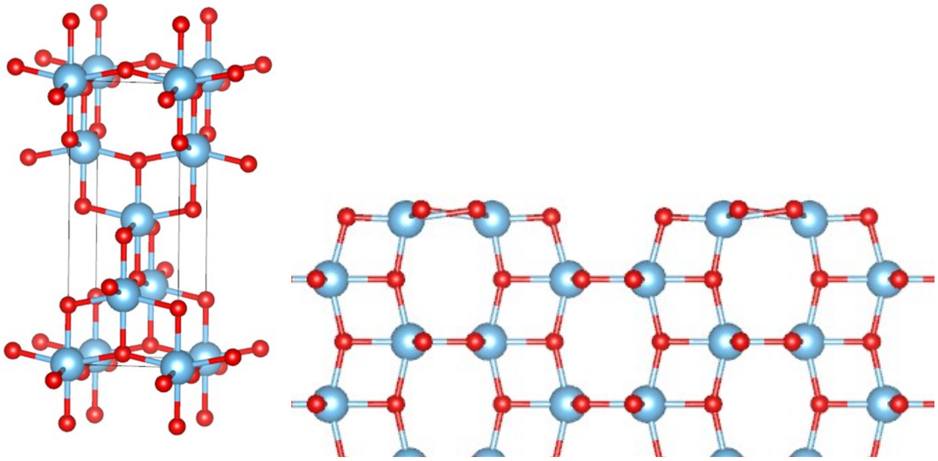

Fig. S12. The model of optimized unit cell of TiO_2 and model of relaxed (1 0 0) surface of TiO_2.

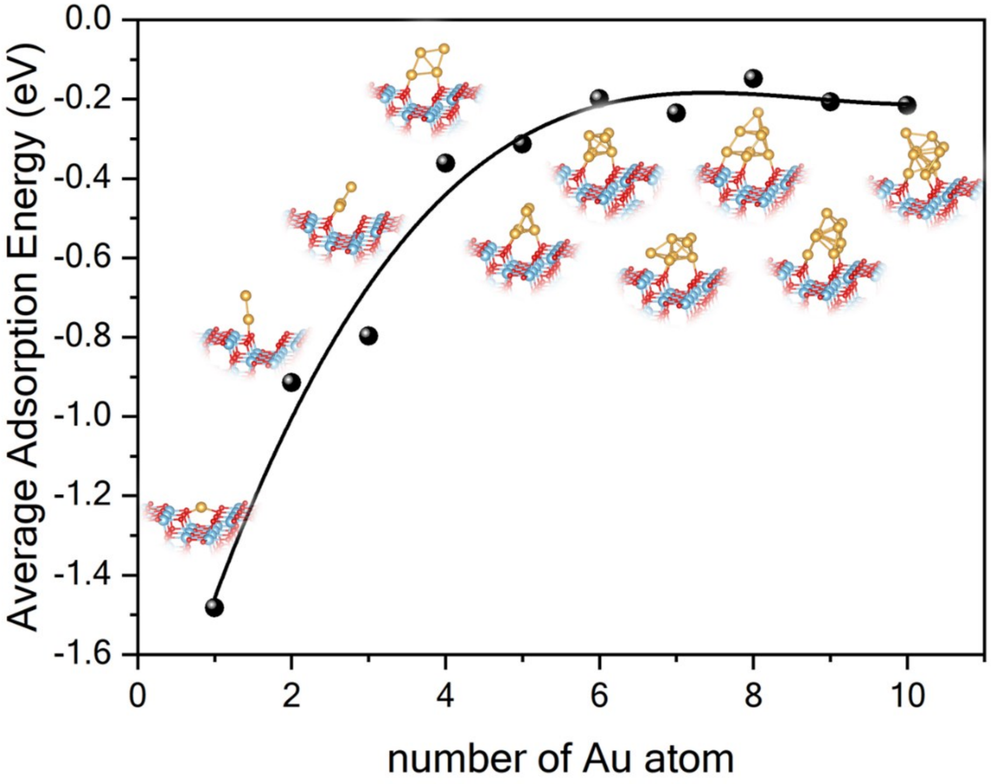

Fig. S13. The average adsorption energy and the optimized models of Au_n/TiO_2 as a function of Au atom number in Au_n cluster.

Au_n/TiO_2 with large n was usually used to simulate the interface structure of Au and TiO_2 in previous studies [15, 16]. The average adsorption energy of Au_n/TiO_2 was used to estimate the size effect of Au cluster. As shown in **Fig. S13**, the average adsorption energy initially decreased rapidly from -1.48 eV in Au_1/TiO_2 to -0.20 eV in Au_6/TiO_2, and then remained in a range from -0.23 to -0.15 eV. For Au_n/TiO_2 with $n \geq 6$, the size effect can be ignored because the average adsorption energy fluctuates within a narrow range. Considering the rationality of the structure and the consumption of computing resources, the Au_6/TiO_2 was chosen for the next mechanism study.

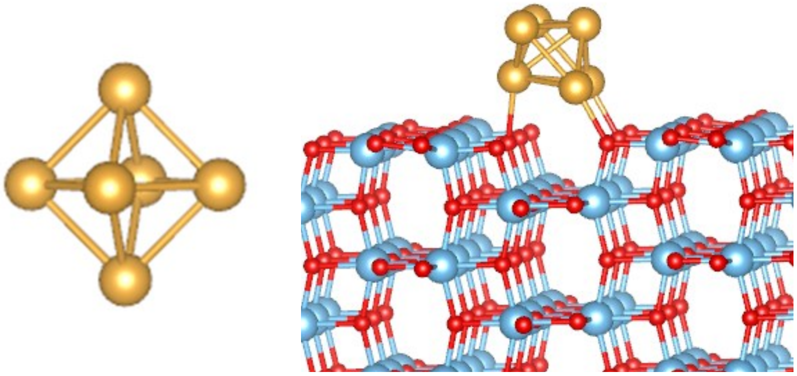

Fig. S14. The model of Au_6 cluster and the optimized interface model of Au/TiO_2.

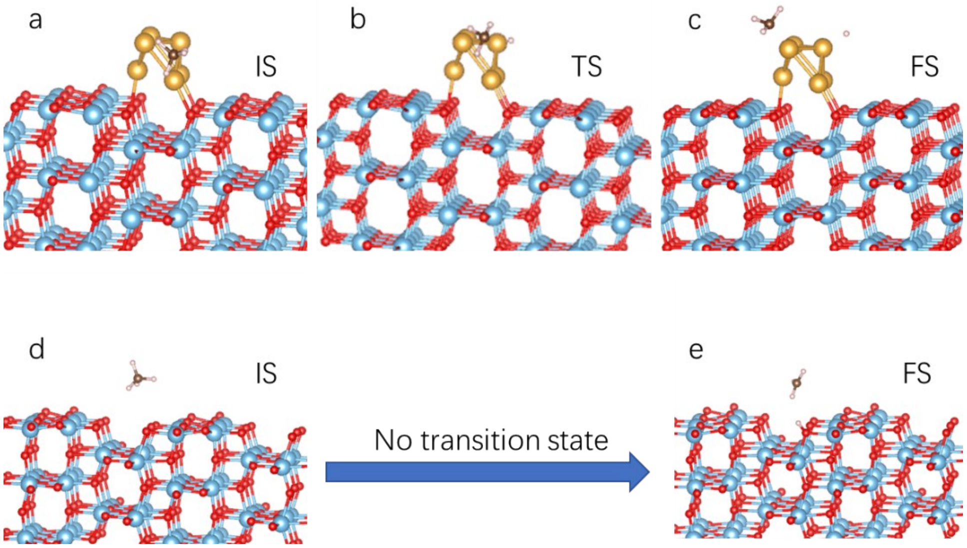

Fig. S15. The models of CH_4 activation section: (a) (b) (c) are the initial state, transition state and final state on Au/TiO_2; (d) (e) are the initial state and final state on surface of TiO_2. According the DFT calculation, there is no transition state in the process of CH_4 activation over the surface of TiO_2.

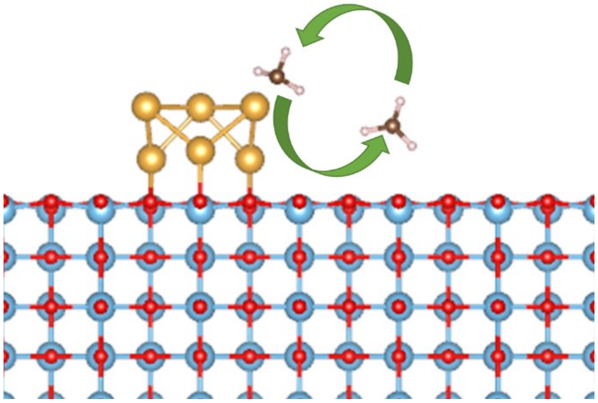

Fig. S16. The model of CH_3 ion migration section

The barriers of CH_3 ions migration were calculated using the climbing image nudged elastic band method (CI-NEB). The surface supercell was enlarged to (6 × 2) for CH_3 ion migration with a vacuum layer of 20 angstroms. The minimum energy paths of CH_3 ion migration were determined with six images between starting point and destination of the migration process presented.

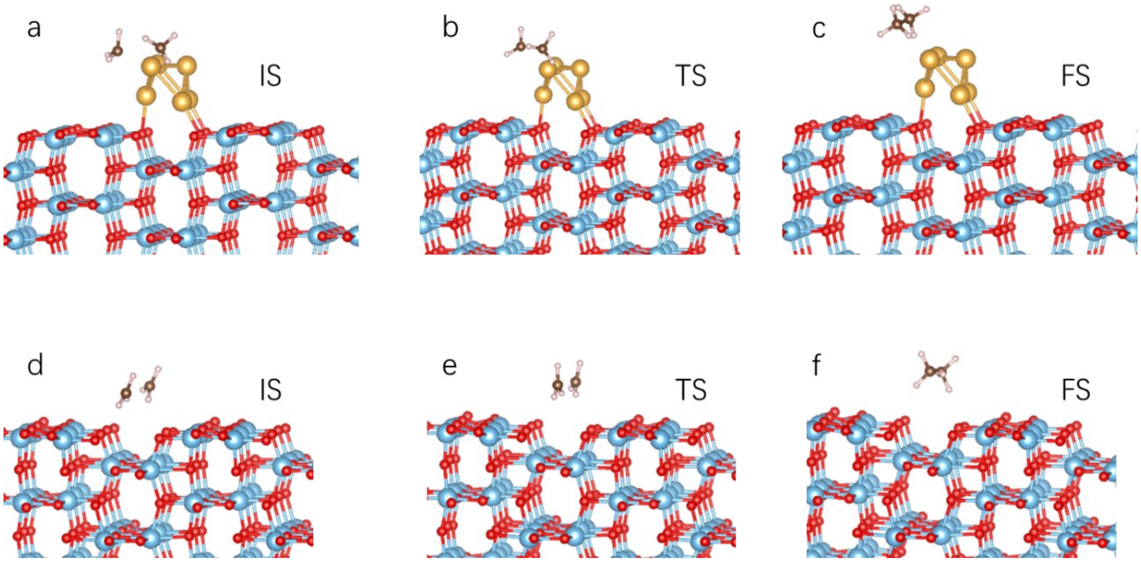

Fig. S17. The models of C_2H_6 formation section: (a), (b), and (c) are the initial state, transition state, and final state on Au/TiO_2; (d), (e), and (f) are the initial state, transition state, and final state on the surface of TiO_2.

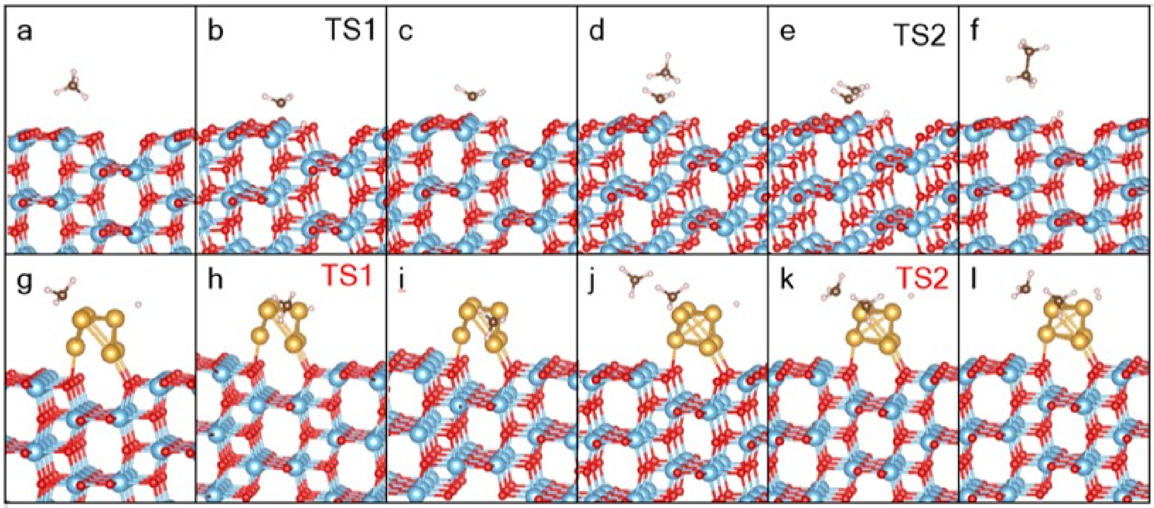

Fig. S18. The models of competitive mechanism **A** (a-f) and competitive mechanism **B** (g-l).

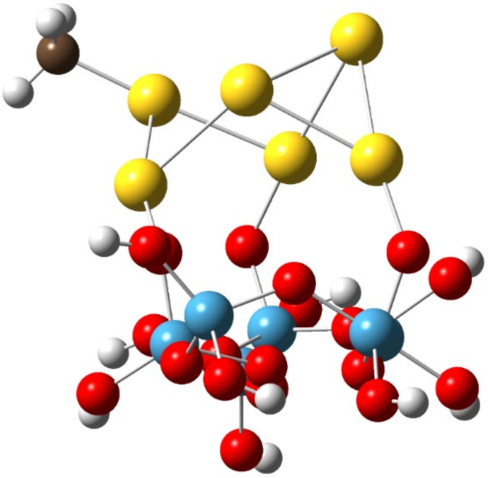

Fig. S19. The model of CH_3-Au/TiO_2 for IR spectrum simulation. Yellow, blue, red, brown, and white balls represent Au, Ti, O, C and H atoms, respectively.

The model consists of Au_6 cluster, TiO_2 cluster, and CH_3 group. The terminal O atoms were coordinately saturated by H atoms. The simulated IR spectrum was obtained from a frequency calculation using Gaussian software. As shown in the orange line of **Fig. 6**, the simulated IR response at about 600-800 cm^{-1} was very similar to the actual IR signal, which demonstrates the existence of methyl anion during the photocatalytic NOCM process.

14. Bader charge analysis

The bader charge analysis was carried out based on DFT calculations and the results were listed in **Table S4**. We constructed a model (**Fig. S15a**) containing a $[CH_3+H]$ group with negative charge on the Au-TiO_2 surface to describe the situation of Reactions **a** and **b**. It is noted that the bader charge of C atom was about 4.32 e approximately equaling to the charge of CH_3^- on Au-TiO_2 model, which indicates Reaction **a** is described for the NOCM reaction. On the other hand, the bader charge analysis of a model (**Fig. S15d**) containing a $[CH_3+H]$ group with negative charge on the TiO_2 surface was also performed. The bader charge of C atom has about 4.34 e, indicating that Reaction **a** can also occur on TiO_2 rather than reaction **b**. Similarly, a model containing a $[CH_3+H]$ group with positive charge on the TiO_2 surface was built to distinguish Reactions c and d. Therefore, the CH_3 species as CH_3^- on Au or CH_3^+ on TiO_2 indicated that the CH_4 molecule was activated in CH_3^-/ CH_3^+ process rather than methyl radical process.

Table S4. Bader charge analysis results

Models	Bader charge of C atom (e)
$[CH_3+H]^-$ on Au-TiO_2	4.32
CH_3^+ on Au-TiO_2	4.25
$\cdot CH_3$ on Au-TiO_2	4.18
CH_3^- on Au-TiO_2	4.31
$[CH_3+H]^+$ on TiO_2	4.21
$[CH_3+H]^-$ on TiO_2	4.34
CH_3^+ on TiO_2	4.20
$\cdot CH_3$ on TiO_2	4.25
CH_3^- on TiO_2	4.38

15. Comparison of the CH_3 anion mechanisms with other reported mechanisms

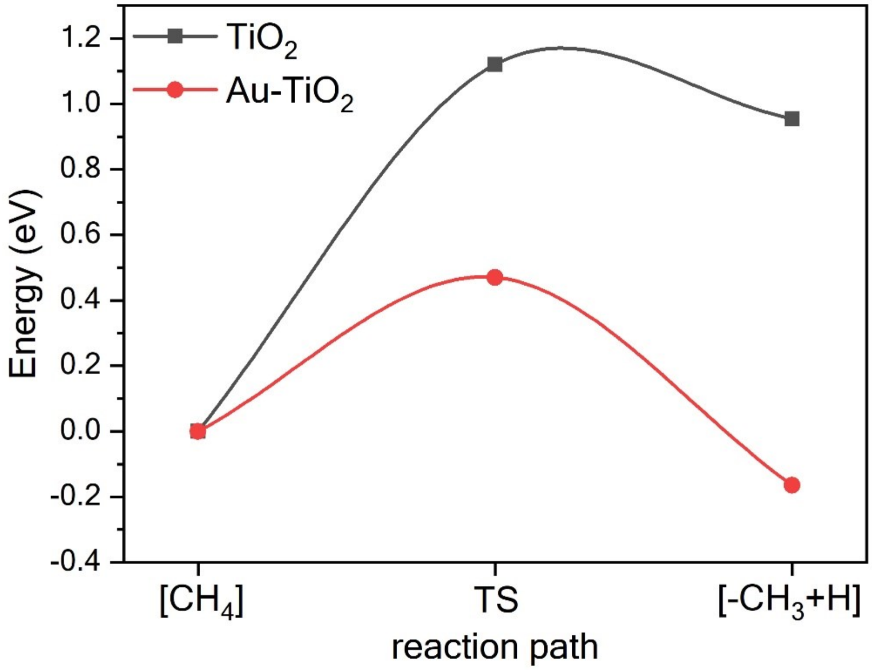

Fig. S20. Detailed free energy diagrams of CH_4 activation over different surfaces.

In order to distinguish whether the reaction **a** occurred on the TiO_2 site or Au site of Au/TiO_2, we performed a DFT calculation of CH_4 activation on the different surfaces (**Fig. S20**). The barrier energy of reaction a on TiO_2 site of Au/TiO_2 was about 1.1 eV, which is larger than that occurs on the Au site of Au/TiO_2. Therefore, CH_4 molecule was preferentially activated on the Au of Au/TiO_2 in the form of reaction **a**.

In literature, two general types of mechanisms were proposed for photocatalytic NOCM, which are summarized as follows:

A. CH_4 is firstly adsorbed on the surface of the oxide to dissociate into CH_3 and H species. Then, the CH_3 species react with photogenerated hole/electron to generate CH_3 radical. Finally, the CH_3 radical combines another CH_4 molecule or CH_3 radical to form C_2H_6. This mechanism was proposed for NOCM over Au/ZnO [13] and Ga-ETS [12] systems.

B. Another type of mechanism considered the effect of reactive metal for photocatalytic NOCM over Pt/TiO_2-SiO_2 [17]. Namely, after adsorbing on the metal atom, a CH_4 molecule is splitting to form a CH_3 radial by light irradiation. Then, another CH_4 molecule is adsorbed on the same metal atom to yield a CH_3 radical via the same photocatalytic process. Finally, two CH_3 radicals combine to generate a C_2H_6.

Those two general types of mechanisms were evaluated for NOCM over Au/TiO_2 and compared with the CH_3 anion mechanism. As shown in **Fig. S21**, the mechanism **A** has the largest reaction barrier (2.56 eV) because the absent of active sites for CH_4 dissociation. Furthermore, in mechanism **B**, although the metal (as an active center) can facilitate the activation of CH_4, the activation barrier for the 2^{nd} CH_4 molecule is about 1.86 eV, which is larger than that of CH_3 anion migration barrier. This indicates that the CH_3 anion mechanism is better to match the NOCM over Au/TiO_2 than other two types of mechanisms.

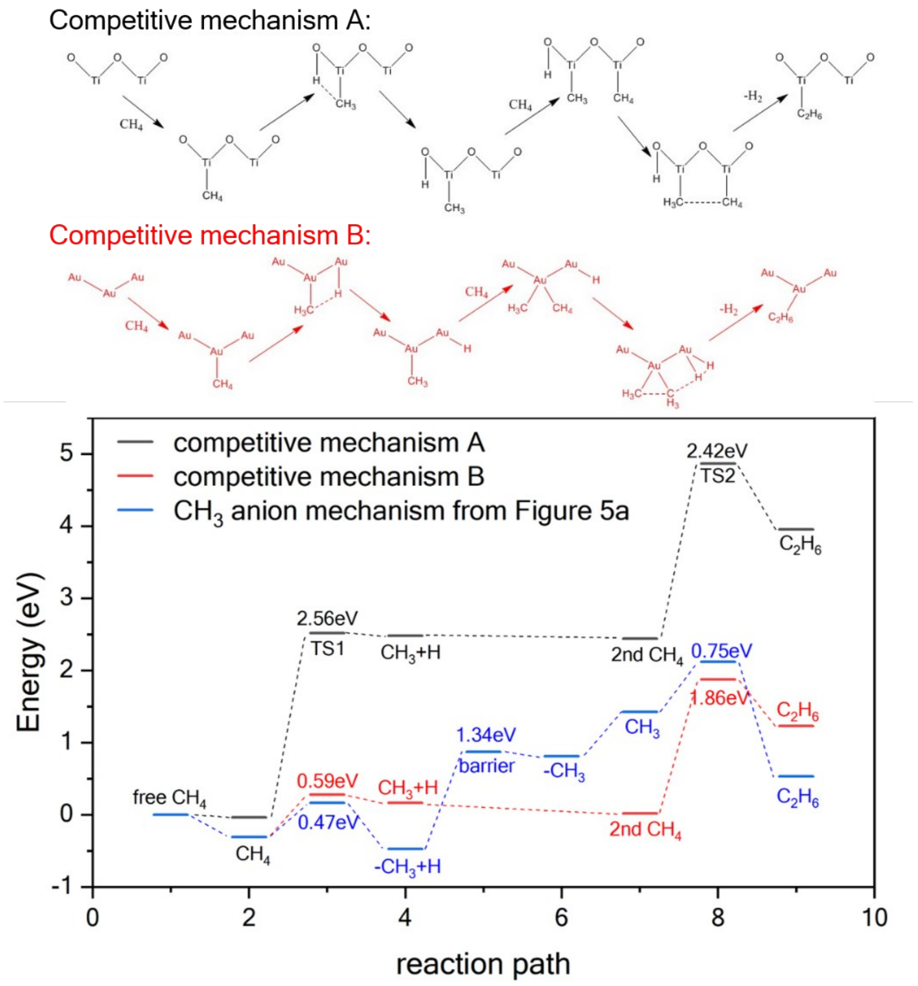

Fig. S21. Comparison between various mechanisms for NOCM over Au/TiO_2 from DFT calculations.

References

1. Y. Zhou, L. Zhang and W. Wang, *Nat Commun*, 2019, **10**, 1-8.
2. L. Yu, Y. Shao and D. Li, *Appl. Catal., B*, 2017, **204**, 216-223.
3. Y. Kato, H. Yoshida and T. Hattori, *Chem. Commun.*, 1998, 2389-2390.
4. Y. Kato, H. Yoshida, A. Satsuma and T. Hattori, *Microporous Mesoporous Mater.*, 2002, **51**, 223-231.
5. H. Yoshida, N. Matsushita, Y. Kato and T. Hattori, *J. Phys. Chem. B*, 2003, **107**, 8355-8362.
6. L. Yuliati, T. Hattori and H. Yoshida, *PCCP*, 2005, **7**, 195-201.
7. L. Yuliati, M. Tsubota, A. Satsuma, H. Itoh and H. Yoshida, *J. Catal.*, 2006, **238**, 214-220.
8. L. Yuliati, H. Itoh and H. Yoshida, *Chem. Phys. Lett.*, 2008, **452**, 178-182.
9. L. Yuliati, T. Hamajima, T. Hattori and H. Yoshida, *J. Phys. Chem. C*, 2008, **112**, 7223-7232.
10. L. Yuliati, T. Hattori, H. Itoh and H. Yoshida, *J. Catal.*, 2008, **257**, 396-402.
11. L. Li, G. D. Li, C. Yan, X. Y. Mu, X. L. Pan, X. X. Zou, K. X. Wang and J. S. Chen, *Angew. Chem. Int. Ed.*, 2011, **50**, 8299-8303.
12. L. Li, Y. Y. Cai, G. D. Li, X. Y. Mu, K. X. Wang and J. S. Chen, *Angew. Chem. Int. Ed.*, 2012, **51**, 4702-4706.
13. L. Meng, Z. Chen, Z. Ma, S. He, Y. Hou, H.-H. Li, R. Yuan, X.-H. Huang, X. Wang and X. Wang, *Energy & Environmental Science*, 2018, **11**, 294-298.
14. C. Yang and Z.-Y. Zhao, *Comput. Mater. Sci.*, 2018, **151**, 160-173.
15. Y.-G. Wang, Y. Yoon, V.-A. Glezakou, J. Li and R. Rousseau, *J. Am. Chem. Soc.*, 2013, **135**, 10673-10683.
16. J. Wang and B. Hammer, *Phys. Rev. Lett.*, 2006, **97**, 136107.
17. S. Wu, X. Tan, J. Lei, H. Chen, L. Wang and J. Zhang, *J. Am. Chem. Soc.*, 2019, **141**, 6592-6600.